frontiers | Frontiers in Materials

TYPE Original Research
PUBLISHED 11 November 2022
DOI 10.3389/fmats.2022.978025

Check for updates

OPEN ACCESS

EDITED BY
Yu-Hong Zhao,
North University of China, China

REVIEWED BY
Qing Wang,
Dalian University of Technology, China
Zhiqin Wen,
Guilin University of Technology, China

*CORRESPONDENCE
Ming Chen,
chenming@ustl.edu.cn

SPECIALTY SECTION
This article was submitted to Computational Materials Science, a section of the journal Frontiers in Materials

RECEIVED 25 June 2022
ACCEPTED 05 October 2022
PUBLISHED 11 November 2022

CITATION
Liu Q, Jiang J, Chen M, Deng X, Wang J and Ju D (2022), Study on the mechanism of carbide precipitation by surface quenching treatment on GCr15 bearing rings based on the phase-field method.
Front. Mater. 9:978025.
doi: 10.3389/fmats.2022.978025

COPYRIGHT
© 2022 Liu, Jiang, Chen, Deng, Wang and Ju. This is an open-access article distributed under the terms of the Creative Commons Attribution License (CC BY). The use, distribution or reproduction in other forums is permitted, provided the original author(s) and the copyright owner(s) are credited and that the original publication in this journal is cited, in accordance with accepted academic practice. No use, distribution or reproduction is permitted which does not comply with these terms.

Study on the mechanism of carbide precipitation by surface quenching treatment on GCr15 bearing rings based on the phase-field method

Qian Liu[1], Jiaxuan Jiang[2], Ming Chen[2]*, Xiaohu Deng[3], Jiangang Wang[4] and Dongying Ju[5]

[1]School of Materials and Metallurgy, University of Science and Technology Liaoning, Anshan, China, [2]School of Mechanical Engineering and Automation, University of Science and Technology Liaoning, Anshan, China, [3]National Local Joint Engineering Laboratory of Intelligent Manufacturing Oriented Automobile Die & Mold, Tianjin University of Technology and Education, Tianjin, China, [4]College of Material Science and Engineering, Hebei University of Science and Technology, Shijiazhuang, China, [5]Saitama Institute of Technology, Fukaya, Japan

In this paper, the thermodynamics database describing Gibbs free energy of *FCC* phase and $M_{23}C_6$ phase based on *Fe-Cr-C* ternary alloy was coupled into phase field simulation, and the phase field model was developed on the mesoscopic scale which simulates precipitation, growth and coarsening of $M_{23}C_6$ carbides in *FCC* austenitic matrix by considering the elastic energy. As the boundary condition of imported phase field calculation, the heat treatment COSMAP software was applied to obtain the macro numerical simulation results of quenching. The phase composition, element distribution, and the evolution including the nucleation, growth and coarsening was simulated by phase field method for the $M_{23}C_6$ carbides in quenching process of GCr15 bearing ring. By means of comparison between the calculation results of phase field simulation and the morphology, quantity and distribution of carbides observed by SEM experiment, this paper present the mechanism on precipitation of micro $M_{23}C_6$ carbides influenced by quenching process parameters, and the experiment verifies the feasibility and accuracy of phase field simulation.

KEYWORDS

phase-field method, carbide, GCr15 bearing steel, elastic properties, quenching, phase change

1 Introduction

Bearings have already been indispensable core components in many areas, such as aerospace, high-speed rail, and the automotive industry. In practical application, a bearing has been designed to withstand cyclical loads and resist external shocks. The purpose has provided an important guarantee for the high rotational accuracy and high wear resistance of many rotary machines at high speeds (Zhao-kun et al., 2016; Zou, 2021). In the manufactured process of bearing, metallurgy, and preparation of the material, the processing technology of

materials and heat treatment technology have been the main factors affecting bearing performance. The bearing ring is the main part. The quenching process of the bearing ring has been very important in determining the final strength, wear resistance, rotation accuracy, and rotation noise performance because it is close to the last process of manufacturing the bearing ring.

High-carbon–chromium bearing steel has good fatigue resistance, elasticity, and toughness. After quenching, it could have high and uniform hardness (Laing et al., 1967). The distribution and composition of carbides have an important influence on the properties of bearing steel. Research on it has been difficult at present, providing a basis for improving the bearing ring dimensional stability and optimizing the heat treatment process (Zong et al., 2020). GCr15 is high-carbon–chromium earing steel. $M_{23}C_6$ are the main carbides in GCr15. Their phase composition, element distribution, and evolution, including nucleation, growth, and coarsening, have an important influence on the dimensional stability of the bearing outer ring (Du, 2017). And $\gamma \rightarrow M_{23}C_6$, the organization and distribution of M23C6 would be influenced by the phase transformation mechanism of GCr15, so to study the phase transformation mechanism of the carbide educt be revealed from *FCC* phase of $M_{23}C_6$ is great significance. The study of the effect of quenching treatment of GCr15 steel on the $\gamma \rightarrow M_{23}C_6$ phase transformation mechanism is of practical guidance.

The phase-field method is a powerful mesoscale calculation method based on density. Based on the concept of MGI, the phase-field method simulates organizational evolution, realizes the prediction of material properties, and accelerates the material development process (Li, 2009; Ding, 2019). Xin et al. provided compelling morphological, chemical, structural, and thermodynamic evidence for the spinodal decomposition and showed that the lattice mismatch at the diffuse transition region between the spinodal zones and matrix is the dominating factor for enhancing yield strength in this class of alloy (Xin et al., 2021). Zhao et al. studied the multi-controlling factors of the dendritic growth in directional solidification through the phase-field method. The effects of the temperature gradient, propelling velocity, thermal disturbance, and growth orientation angle on the growth morphology of the dendritic growth at the solid/liquid interface were discussed (Zhao et al., 2019). Zhang et al. (2018) developed a model of rapid solidification of non-stoichiometric intermetallic compounds based on the thermodynamic extremal principle, and the *Co-xat. %Si* alloys (*x ¼ 50, 53, 55*) were undercooled to test the model. Kuang et al. (2018) considered the thermodynamic extremal principle and proposed a modified quasi-sharp-interface model that integrates trans-interface diffusion from the product phase to the interface, trans-interface diffusion from the interface to the parent phase, and interface migration and bulk diffusion of *C* and *X*. Applications to isothermal and cyclic phase transformations showed that the model allows the arbitrary setting of the initial conditions. Zhao et al. used a multi-component continuous phase-field model based on the Gibbs free energy of the sub-regular solution. The core-shell structure precipitates of *Fe-xCu-3.0Mn-1.5Ni-1.5Al* alloys under internal and external strain were investigated (Zhao et al., 2022a). Tian et al. (2022) used the phase-field-crystal method and dynamically displayed the interaction between twins and dislocations. In this study, the phase-field method was used to study the effect of the precipitation mechanism of $M_{23}C_6$ carbides during bearing ring quenching. First, COSMAP was used to simulate the GCr15 bearing ring quenched to obtain elastic field data. The heat treatment simulation results were introduced into the phase-field model to obtain the nucleation, growth, and coarsening process of $M_{23}C_6$ carbides precipitated from the *FCC* matrix phase under the influence of coupling elastic energy and describe the morphology and distribution of $M_{23}C_6$ carbides in the *FCC* matrix phase. Finally, the morphology and distribution of $M_{23}C_6$ carbides in the quenched GCr15 bearing ring were tested by SEM, and the phase-field simulation and experimental results were compared.

2 Multi-field coupling quenching process simulation

The research sample is the bearing ring, and the material is GCr15. The workflow is as follows: first, it completes model preprocessing by GID and then analyzes the material properties. These are preparations for the next numerical simulation. The main focus of the quenching process is the deformation problem for the bearing ring. The temperature field variation and deformation behavior could be analyzed. The simulation process by COSMAP is shown in Figure 1.

2.1 Geometric model

The specimen's critical dimensions are a diameter of 125 mm, a wall thickness of 7.5 mm, and a width of 11 mm. It belongs to the thin-walled part.

2.2 Building a finite element model

As shown in Figure 2, analytical model had been created 16,611 nodes and 13,328 cells. On the section of the bearing model, there are three points, called P1, P2, P3, and P1 node represent endpoint of the outer ring, P2 node represent endpoint of the middle surface and P3 node represent endpoint of the inner surface. These three nodes move along the arc and vertical direction and divided the model into hexahedral elements of similar size for the calculation units of finite element analysis. The purpose is to determine the temperature *f* variation and deformation at different positions and accurately describe the deformation behavior of the quenched bearing ring.

2.3 Quenching process

The experimental heat treatment process is heating for 15 min to 845°C, then holding for 25 min, and finally quenching in oil.

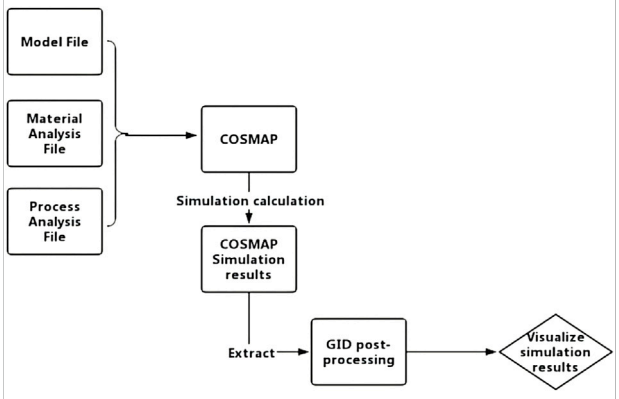

FIGURE 1
Flowchart of COSMAP simulation.

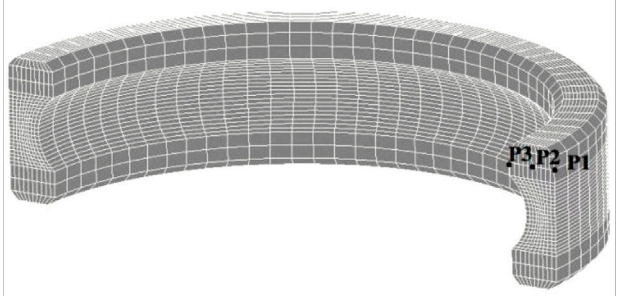

FIGURE 2
Diagram of the analysis area based on the model meshed.

According to experience, the heat transfer law of the ring has been set, and the adopted values are shown in Figure 3. The heat transfer coefficient curve could accurately reflect the temperature cooling in oil quenching, compared with the oil cooling curve (Liu et al., 2022) Table 1 shows the chemical composition of GCr15 used in the analysis.

2.4 Simulation results and analysis

Temperature variation and deformation law are listed in this study. From Figure 4, the results of temperature cooling in various regions of the ring quenched could be analyzed. Temperature cooling varies for the interior and surface of the bearing ring entity. Because the surface has direct contact with the oil, its cooling rate is faster. The heat transfer between the surface and the interior is heat conduction; there is a certain time difference, so the internal cooling rate is slow. There is no obvious temperature difference between the inner and outer surfaces for the thin-walled part. Temperature difference at different locations is likely to affect carbide formation, distribution, and coarsening. It could be verified in the subsequent phase-field simulation and test.

Studying the deformation mechanism of the quenched bearing outer ring is always difficult. Although the ovality of the outer ring can be adjusted by subsequent processing, the dimensional stability is an unresolved fundamental problem for long-term applications, which affects the performance of bearings. Therefore, how to better control the deformation of the heat treatment process is still a topic of research in the industry.

The variation trend of deformation can be obtained from Figure 5. When the cooling rate is the fastest, the deformation is reduced to the lowest. After about 6 s, a parabolic trend appears, which is affected by the latent heat of phase change. In the convective heat transfer stage, the deformation tends to be stable.

3 Phase-field simulation

The precipitation process of carbides from phases in GCr15 bearing steel was simulated by the phase-field method. The influence of elastic energy on the $\gamma \rightarrow M_{23}C_6$ phase transition mechanism is also considered.

4 Flowchart for introducing elastic energy in phase-field simulation

Figure 6 shows the analysis process of elastic strain energy introduction.

4.1 Establishment of the phase-field model

Because there are many kinds of elements in GCr15 bearing steel and our phase-field simulation program only supports the ternary alloy system, three main elements (Fe, Cr, and C) in GCr15 steel are selected. Independent component field variables $c_i(r,t)(i=1,2,3)$ and single-ordered parameter $\phi(r,t)$ have been used to describe its microstructure evolution. In the formula $c_i(r,t)(i=1,2,3)$, where it represents, respectively, instantaneous concentrations of Fe, Cr, and C atoms in specific spatial positions r at some times t. Order parameters $\phi(r,t)$ represent phase distribution in specific spatial positions, and $h(\phi)$ ranges from 0 to 1, where $h(\phi)=0$ corresponds to the *FCC* structural phase and $h(\phi)=1$ corresponds to the $M_{23}C_6$ phase. It mainly expresses the carbide phase transformation process. The phase-field model can be analyzed using Eqs. 1, 2 as follows:

$$\frac{\partial c_i(r,t)}{\partial t} = \sum_j \left(M_i \nabla^2 \frac{\delta F}{\delta c_j(r,t)} \right) + \xi_{c_i}(r,t), i = j = Cr, C, \quad (1)$$

$$\frac{\partial \phi(r,t)}{\partial t} = -L \frac{\delta F}{\delta \phi(r,t)} + \xi_{\phi}(r,t), \quad (2)$$

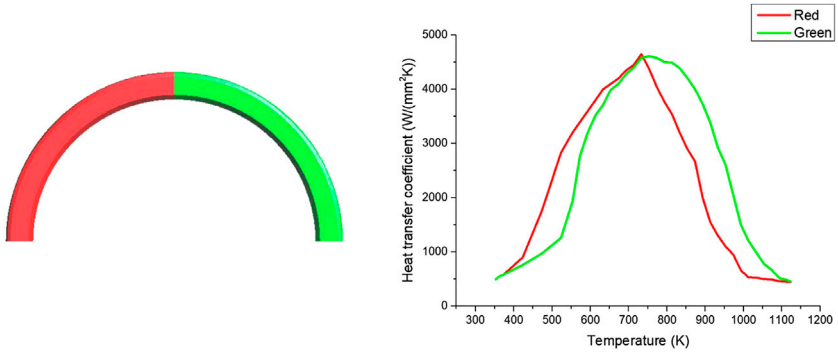

FIGURE 3
Surface heat transfer coefficient law of GCr15 steel quenched in oil.

TABLE 1 Chemical composition of GCr15 steel.

Ingredient	C	Si	P	S	Fe
Mass fraction (%)	0.95–1.05	0.15–0.35	0.25	0.25	Bal
Ingredients	Cr	Mn	Mo	Ni	Cu
Mass fraction (%)	1.40–1.65	0.25–0.45	≤ 0.1	0.30	0.25

where $\xi_{c_j}(r,t)$ and $\xi_{\phi}(r,t)$ represent the Gauss noise term from the fluctuation–dissipation theorem (Guo, 2021). They are added to the equation to cause small component fluctuations and provide initial energy for the occurrence of the phase transition process. The parameter L represents the kinetic coefficient of phase transition, which can be used to characterize the phase transition evolution between the *FCC* and $M_{23}C_6$ phases (Hu et al., 2007). It has been simplified as a constant in the analytical process. The parameter F represents the total free energy of the microstructure. Contributions of local chemical free energy, gradient energy, and elastic strain energy have been considered simultaneously. Eq. 3 is used to calculate the total free energy F of the system. M_i represents the diffusion mobility of effective components in the alloy system and is analyzed in Eq. 4 (Zhu et al., 2004; Koyama and Onodera, 2005):

$$F = \int_v f dv = \int_v \left[\frac{f_{local}(c,\phi,T)}{V_m} + f_{grad} + \frac{f_{el}}{V_m} \right] dV, \quad (3)$$

where f_{local}, f_{grad}, and f_{el} represent local chemical free energy, gradient energy (Cahn and Hilliard, 1958), and elastic strain energy, respectively. The parameter V represents the volume of the system.

$$M_i = h(\phi) \cdot M_{M_{23}C_6} + (1 - h(\phi)) M_{fcc}, \text{the i} = \text{Cr, C}, \quad (4)$$

where $M_{M_{23}C_6}$ represents the atomic diffusion mobility of the Cr and C atoms in the $M_{23}C_6$ phase and M_{fcc} represents the atomic diffusion mobility of the Cr and C atoms in the FCC phase. Eq. 5 can be used to calculate the following:

$$M_\phi = \frac{D_\phi^{self}}{RT}, \quad (5)$$

where parameter R represents the gas constant (Jiang et al., 2022), $R = 8.314472\text{J}/(\text{mol} \cdot \text{k})$. The parameter T represents temperature. D_ϕ^{self} represents self-diffusion coefficient and has been calculated using Eq. 6:

$$D_\phi^{self} = D_0 \, exp\left(-\frac{Q}{RT}\right), \quad (6)$$

where the parameter Q represents diffusion activation energy and the parameter D_0 represents the frequency factor.

Available kinetic parameters have been referred to in Table 2.

4.2 Local chemical free energy

The Wheeler et al. (1992) (WBM) model has been applied to the analysis. Local chemical free energy can be considered by combining two single-phase free energies:

$$f_{local}(c,\phi,T) = \frac{1}{V_m}\left\{h(\phi)G_m^{M_{23}C_6} + [1 - h(\phi)]G_m^{fcc} + \omega g(\phi)\right\}. \quad (7)$$

V_m represents the molar volume of the system (Zhu et al., 2011); the value can be referred to in Table 2. c represents the mass percentage of the solute atom. The value of ϕ equals 0 in the *FCC* phase and 1 in the $M_{23}C_6$ phase. The parameter T represents temperature. ω represents the height of the potential well and has been used to analyze the resistance, which needs to be overcome for phase transformation (Koyama et al., 2006; Zhao et al., 2022b). Two continuous interpolation functions $g(\phi)$ and $h(\phi)$ have value in the range of 0–1 (Koyama et al., 2006; Zhao, 2022). The function of $h(\phi)$ has mainly reflected the smooth transition of the precipitated phase from the *FCC* phase to the $M_{23}C_6$ phase. $g(\phi)$ has been applied in the form

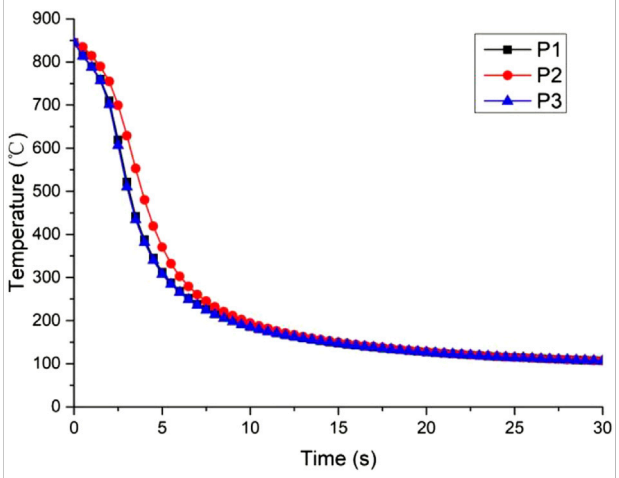

FIGURE 4
Cooling curves of different nodes during quenching of the GCr15 bearing ring.

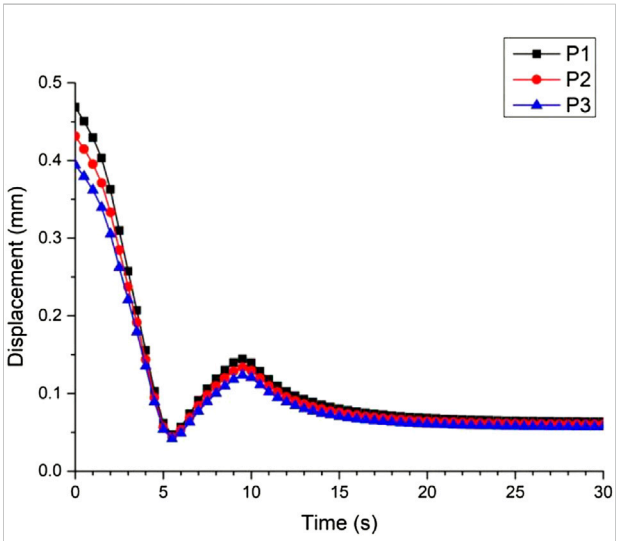

FIGURE 5
Curve of deformation in quenching.

of double-well potential and represented an energy barrier for phase transition. They can be analyzed, respectively, through Eqs. 8, 9. $G_m^{M_{23}C_6}$ and G_m^{fcc} represent the molar Gibbs free energy of the *FCC* and $M_{23}C_6$ phases, respectively:

$$g(\phi) = \phi^2(1-\phi^2), \tag{8}$$

$$h(\phi) = \phi^3(6\phi^2 - 15\phi + 10). \tag{9}$$

The relationship between them can be derived from Eq. 10 (Loginova et al., 2003):

$$\frac{dh(\phi)}{d\phi} = 30g(\phi). \tag{10}$$

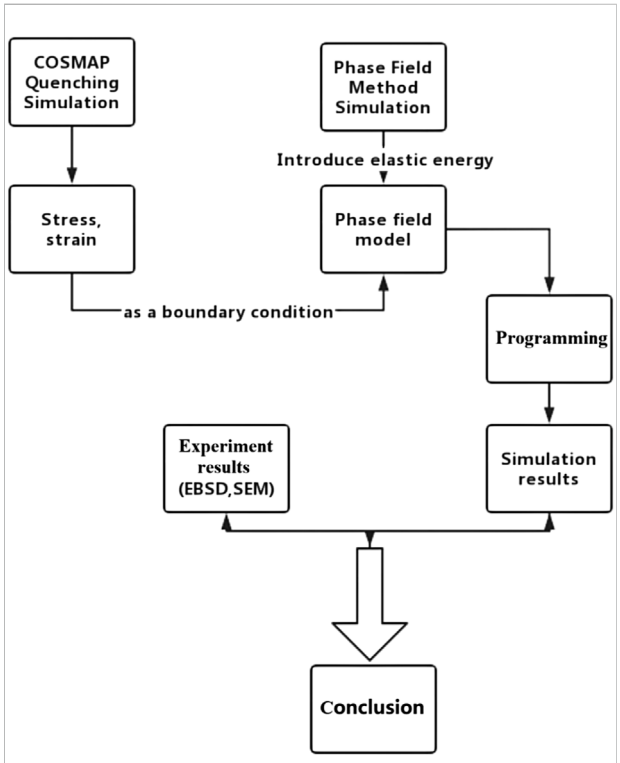

FIGURE 6
Flowchart for the introduction of elastic energy.

Based on the CALPHAD method (Saunders and Miodownik, 1992), the molar Gibbs free energy of the *FCC* matrix phase can be described through two sub-lattice models (Fe, Cr) and (C, Va). Metal elements have been mixed in the first sublattice and carbon and vacancy in the interstitial sub-lattice (Andersson, 1988; Khvan et al., 2014):

$$\begin{aligned} G_m^{fcc} = {} & y_{Fe}y_c{}^0G_{Fe,c}^{fcc} + y_{Fe}y_{va}{}^0G_{Fe,va}^{fcc} + y_{Cr}y_c{}^0G_{Cr,c}^{fcc} + y_{Cr}y_{va}{}^0G_{Cr,va}^{fcc} \\ & + RT(y_{Fe}\ln y_{Fe} + y_{Cr}\ln y_{Cr}) + RT(y_{va}\ln y_{va} + y_c\ln y_c) \\ & + {}^EG_m^{fcc}, \end{aligned} \tag{11}$$

where

$$\begin{aligned} {}^EG_m^{fcc} = {} & y_{Fe}y_{Cr}\left(y_cL_{Cr,Fe:\,c}^{fcc} + y_{va}L_{Cr,Fe:\,va}^{fcc}\right) + y_{va}y_c\left(y_{Cr}L_{Cr:\,va,c}^{fcc}\right. \\ & \left. + y_{Fe}L_{Fe:\,va,c}^{fcc}\right). \end{aligned} \tag{12}$$

y_i represents the lattice fraction of the *Ith* component between metallic and interstitial sub-lattices. The parameter L is an interaction parameter related to the concentration. ${}^0G_{i:\,va}^{fcc}$ represents the Gibbs free energy of the *Ith* pure component under the assumed non-magnetic state. ${}^0G_{i:\,c}^{fcc}$ represents the Gibbs free energy in the assumed non-magnetic state when the interstitial position has been completely filled with carbon elements. The relationship between the lattice fraction and molar fractions has been described by Eqs. 13, 14:

TABLE 2 Calculation results of kinetic parameters.

Parameter	Symbol	Value	Unit	Reference
Interface dynamics coefficient	L	1×10^{-5}	$m^3 J^{-1} s^{-1}$	Zhao et al. (2022a)
Molar volume	V_m	7.09×10^{-6}	$m^3 mol^{-1}$	Zhu et al. (2011)
Self-diffusion coefficient $D_\phi^{self} = D_0 exp(-\frac{Q}{RT})$	$D^{self}_{C\,in\,M_{23}C_6}$	$D_0 = 15 \times 10^{-7}$	$m^2 s^{-1}$	Levchenko et al. (2009)
		$Q = 1.8 \times 10^5$		
	$D^{self}_{Cr\,in\,M_{23}C_6}$	8.72×10^{-12}		Song et al. (2014)
	$D^{self}_{C\,in\,fcc}$	$D_0 = (0.146 - 0.36C(1 - 1.075Cr) + K_1 M) \times 10^{-4}$		
		$K_1 = 0$		Lee et al. (2011)
		$Q = (-144.3 - 15.0C + 0.37C^2 + K_2 M) \times 10^3$		
		$K_2 = 7.7260$		
	$D^{self}_{Cr\,in\,fcc}$	$D_0 = 5.2 \times 10^{-9}$		Kučera and Stránský (1982)
		$Q = 1.8 \times 10^5$		
Elastic constant	C_{ij}	$M_{23}C_6$ { $C_{11} = 471.6$; $C_{12} = 215.7$; $C_{44} = 135.1$ }	Gpa	Liu et al. (2015)
		FCC { $C_{11} = 204.0$; $C_{12} = 133.0$; $C_{44} = 126.0$ }		Kamel and Hafid (2013)

$$y_{Fe} = x_{Fe}/(1 - x_c),\ y_{Fe} + y_{Cr} = 1, \tag{13}$$

$$y_c = x_c/(1 - x_c),\ y_c + y_{va} = 1. \tag{14}$$

Molar free energy of the $M_{23}C_6$ carbide phase has also been treated by two sub-lattice models $(Fe.Cr)_{23}C_6$:

$$G_m^{M_{23}C_6} = y_{Fe}\,{}^0G_{Fe:c}^{M_{23}C_6} + y_{Cr}\,{}^0G_{Cr:c}^{M_{23}C_6} + 7RT(y_{Fe}\,ln\,y_{Fe} + y_{Cr}\,ln\,y_{Cr}) + y_{Fe}y_{Cr}L_{Cr,Fe:c}^{M_{23}C_6}. \tag{15}$$

In Eq. 15, ${}^0G_{i:c}^{M_{23}C_6}$ represents the Gibbs free energy of the pure binary carbide.

All thermodynamic parameters in the molar Gibbs free energy of the *FCC* and $M_{23}C_6$ phases have been calculated (Andersson, 1987; Andersson, 1988; Khvan et al., 2014). Parameter calculation is summarized in Table 3.

The distribution of the molar free energy of the *FCC* and $M_{23}C_6$ phases varying with the lattice fraction has been obtained from Figure 7. Figure 7A shows that the molar free energy of the $M_{23}C_6$ phase decreases with the increase in the sub-lattice fraction of iron and carbon elements, and the molar free energy of the $M_{23}C_6$ phase is minimum when the sub-lattice fraction of iron and carbon elements reaches an equilibrium value. Figure 7B shows that the molar free energy of the *FCC* phase is minimum when the sub-lattice fraction of iron and chromium elements reaches an equilibrium value. Meanwhile, the sub-lattice fraction of the carbon element equals to about 0.5.

4.3 Gradient energy (physics)

The uneven interface composition and difference in structural order parameters should be the main reason for the existence of gradient energy. There is a certain relationship between gradient energy and system interface energy. System interface energy could reflect gradient energy, and details can be explained using Eq. 16.

$$f_{grad} = \frac{1}{2}k_c \sum_j |\nabla c|^2 + \frac{1}{2}k_\phi |\nabla \phi|^2, \tag{16}$$

where k_c defines the gradient energy coefficient of the concentration or composition field and equals 7.05×10^{-9}j/m (Kitashima et al., 2008). k_ϕ defines the gradient energy coefficient of the phase-field or the order parameter and equals 1.4×10^{-10}j/m (Jokisaari and Thornton, 2015).

4.4 Elastic strain energy

The elastic strain energy plays an important role in the morphology, size, and orientation of precipitates and the precipitation kinetic process during the solid-state transformation of alloys. Differences in elastic constants between the new and parent phases, the lattice mismatch between elements or phases, and external stress or strain field should actuate the generation of elastic strain energy and form a stress–strain effect (Sun., 2020; Wu, 2021). For these reasons, strain energy should be added to the total free energy equation to develop the phase-field model, which would study the effect of elastic energy on the solid-state phase transformation process of alloys. Elastic energy in the phase-field model is analyzed using Eq. 17.

$$f_{el} = \frac{1}{2}\int_V \sigma_{ij}\varepsilon_{ij}^{el} dv. \tag{17}$$

In Eq 17, σ_{ij} reflects elastic stress and ε_{ij}^{el} reflects the elastic strain, which has a relation with the total strain ε_{ij} and eigenstrain ε_{ij}^0:

TABLE 3 Calculation parameters of thermodynamic parameters with the *FCC* and $M_{23}C_6$ phases (Andersson, 1987; Andersson, 1988; Khvan et al., 2014).

Phase	Thermodynamic parameter (J/mol)
$M_{23}C_6$	${}^0G^{M_{23}C_6}_{Fe:C} = GFEM23C6$
	${}^0G^{M_{23}C_6}_{Cr:C} = GCRM23C6$
	$L^{M_{23}C_6}_{Cr:Fe:C} = 10434 - 14.281T$
	$GFEM23C6\,(298.15 < T < 6000) = +7.66667GFECEM - 1.666667{}^0G^{graphite}_C + 15000$
	$GCRM23C6\,(298.15 < T < 6000) = -521.983 + 3622.24T - 620.965T\,ln(T) - 0.126431T^2$
	${}^0G^{graphite}_C\,(298.15 < T < 6000) = -17368.441 + 170.73T - 24.3T$ $ln(T) - 4.723E-04T^2 + 2562600T^{-1} - 2.643E+08T^{-2} + 1.2E+10T^{-3}$
	$GFECEM\,(163 < T < 6000) = -10195.860754 + 690.949887637T - 118.47637T\,ln(T) - 0.0007T^2 + 590527T^{-1}$
fcc	${}^0G^{fcc}_{Fe:C} = {}^0G^{fcc}_{Fe} + {}^0G^{graphite}_C + 77207 - 15.877T$
	${}^0G^{fcc}_{Cr:C} = {}^0G^{fcc}_{Cr} + {}^0G^{graphite}_C + 1200 - 1.94T$
	${}^0G^{graphite}_C\,(298.15 < T < 6000) = -17368.441 + 170.73T - 24.3T\,ln(T) - 4.723$ $E-04T^2 + 2562600T^{-1} - 2.643E+08T^{-2} + 1.2E+10T^{-3}$
	$L^{fcc}_{Cr:Fe,C} = -69534 + 3.2353T$
	${}^0L^{fcc}_{Cr,Fe:va} = 10833 - 7.477T$
	${}^1L^{fcc}_{Cr,Fe:va} = 1410$
	$L^{fcc}_{Fe:C,va} = -34671$
	$L^{fcc}_{Cr:va,C} = -29686 - 18T$
	${}^0G^{fcc}_{Fe}\,(298.15 < T < 1811) = -1462.4 + 8.282T - 1.15T\ln(T) + 6.4E-04T^2 + {}^0G^{bcc\_A2}_{Fe}$
	${}^0G^{fcc}_{Cr}\,(298.15 < T < 6000) = {}^0G^{bcc\_A2}_{Cr} + 7284 + 0.163T$
	${}^0G^{bcc\_A2}_{Fe}\,(298.15 < T < 1811) = +1225.7 + 124.134T - 23.5143T\ln(T) - 0.00439752T^2 - 5.8927E-08T^3 + 77359T^{-1}$
	${}^0G^{bcc\_A2}_{Cr}\,(298.15 < T < 2180) = -8856.94 + 157.48T - 26.908T\ln T + 0.00189435T^2 - 1.47721E-06T^3 + 139250T^{-1}$

$$\varepsilon^{el}_{ij} = \varepsilon_{ij} - \varepsilon^0_{ij}. \tag{18}$$

The value of the eigenstrain, which should be calculated through Eq. 19, has been affected by the concentration field:

$$\varepsilon^0_{ij} = \varepsilon^i_0 \delta_{ij}\left(c_i - c^0_i\right), \tag{19}$$

$$\varepsilon^{\mathrm{i}}_0 = \frac{1}{\mathrm{a}}\left(\frac{\mathrm{da}}{\mathrm{dc_i}}\right). \tag{20}$$

ε^i_0 represents the lattice expansion coefficient of the *Ith* element to the matrix element, as described by Eq. 20. The Kronecker delta function δ_{ij} equals 1 when $i = j$. In other cases, it equals 0. c^0_i represents the initial concentration of the *Ith* element.

The total strain ε_{ij} is described by Eq. 21.

$$\varepsilon_{ij} = \frac{1}{2}\left\{\frac{\vartheta u_i}{\vartheta r_j} + \frac{\vartheta u_j}{\vartheta r_i}\right\}, \tag{21}$$

where u represents the displacement field. The parameter r is a vector that reflects the position of the lattice space.

Assuming there is a linear elastic relation between the *FCC* and $M_{23}C_6$ phases, both follow Hook's law. Then,the following equations are derived:

$$\sigma_{ij} = C_{ijkl}\varepsilon^{el}_{kl}, \tag{22}$$

$$f_{el} = \frac{1}{2}\int_V \sigma_{ij}\varepsilon^{el}_{ij}dv = \frac{1}{2}\int_V C_{ijkl}\varepsilon^{el}_{kl}\varepsilon^{el}_{ij}dv. \tag{23}$$

The elastic modulus of the matrix phase is different from that of the precipitated phase. The elastic modulus tensor C_{ijkl} described by Eq. 24 considered the uneven effect of elasticity. The tensor of the elastic modulus depend on the concentration as the Eq. 24 can be shown. So the coefficient of the elastic modulus tensor can be derived form the formula of the concentration field of it. ε^{el}_{ij} represents the elastic strain and is described in Eq. 25.

$$C_{ijkl}(c) = C^{eff}_{ijkl} + \alpha(c)\Delta C_{ijkl}. \tag{24}$$

In Eq. 24, $\alpha(c)$ is the linear function of c, $\alpha(c) = c - c_0$, and c_0 represents the initial concentration value. C^{eff}_{ijkl} represents the average elastic modulus tensor from the elastic modulus tensor of the *FCC* phase, C^{fcc}_{ijkl}, and the $M_{23}C_6$ phase $C^{M_{23}C_6}_{ijkl}$ (Gururajan and Abinandanan, 2007). ΔC_{ijkl} represents the elastic modulus difference and is described by the difference between the elastic modulus tensor of the *FCC* phase, C^{fcc}_{ijkl}, and the $M_{23}C_6$ phase $C^{M_{23}C_6}_{ijkl}$. The uniform elastic system appears when the difference equals 0:

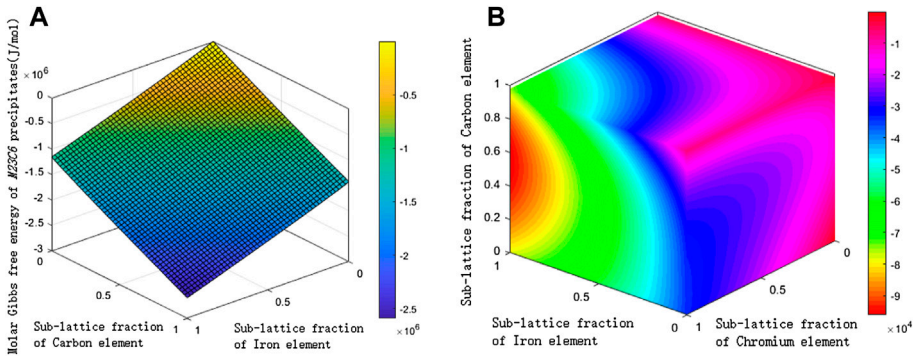

FIGURE 7
Distribution of free energy at 1,073 K. **(A)** $M_{23}C_6$ phase. **(B)** *FCC* matrix phase.

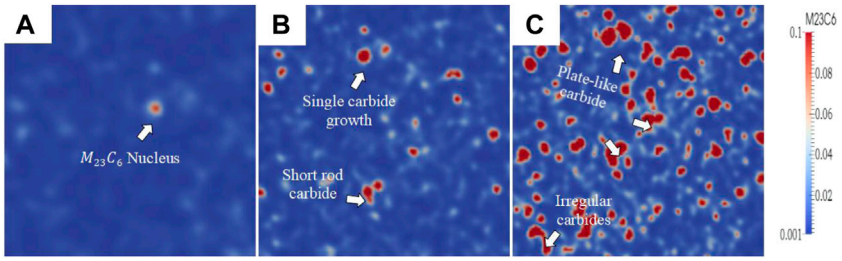

FIGURE 8
Evolution of carbide over time based on 1,123 K. **(A)** t* = 14. **(B)** t* = 15. **(C)** t* = 16.

$$\varepsilon_{ij}^{el} = \varepsilon_{ij}^{a} + \delta\varepsilon_{ij} - \varepsilon_{ij}^{0}. \tag{25}$$

In Eq. 25, ε_{ij}^{a} represents the applied strain and $\delta\varepsilon_{ij}$ represents the internal nonuniform strain. According to Eqs. 22, 24, 25 can evolve into Eq. 26.

$$\sigma_{ij} = \left[C_{ijkl}^{eff} + \alpha(c)\Delta C_{ijkl}\right]\left(\varepsilon_{ij}^{a} + \delta\varepsilon_{ij} - \varepsilon_{ij}^{0}\right). \tag{26}$$

4.5 Phase-field solution

In order to obtain the instantaneous state for the phase-field simulation of the microstructure, the dynamic equations in the phase-field model are solved. As the expression of free energy belongs to the nonlinear equation, the phase-field evolution is mostly to solve the complex nonlinear partial differential equation. At present, there are three methods for solving such complex partial differential equations: the Fourier spectrum method, the finite element method, and the finite difference method (Chen and Jie, 1998). These equations usually have no analytical solution, so an efficient solution has been used to improve the computational efficiency. The Fourier spectral algorithm could transform nonlinear partial differential equations into ordinary differential equations. The Fourier spectral algorithm has eliminated spatial dependence of field variables and realized the Fourier transform rapidly, so computational efficiency achieved improvement. By referring to the factor, the semi-implicit Fourier spectral algorithm has been applied to solving equations in the phase-field model.

Eqs. 27, 28 are obtained by deducing Eqs. 1, 2:

$$\frac{\partial\{c_i(r,t)\}_k}{\partial t} = -k^2\sum\nolimits_J M_{ij}\left\{\left\{\frac{\delta f_{local}}{\delta c_i(r,t)}\right\}_k + \left\{\frac{\delta f_{el}}{\delta c_i(r,t)}\right\}_k + k^2\kappa\{c_i(r,t)\}_k\right\} + \{\xi_{ci}(r,t)\}_k, \tag{27}$$

$$\frac{\partial\{\phi(r,t)\}_k}{\partial t} = -k^2\left\{\frac{\delta f_{local}}{\delta\phi(r,t)}\right\}_k - k^2\kappa L\{\phi(r,t)\}_k + \{\xi_\phi(r,t)\}_k. \tag{28}$$

In Eqs. 27, 28, $\{\cdot\}_k$ represents the Fourier transform. k represents the vector in the Fourier space, and k equals $\sqrt{k_x^2 + k_y^2}$ for the two-dimensional space. κ represents the gradient energy coefficient.

Eqs. 27, 28 are treated by the semi-implicit method, including implicit processing of linear and second-order items and display processing of other items. Eqs. 29, 30 result from this derivation:

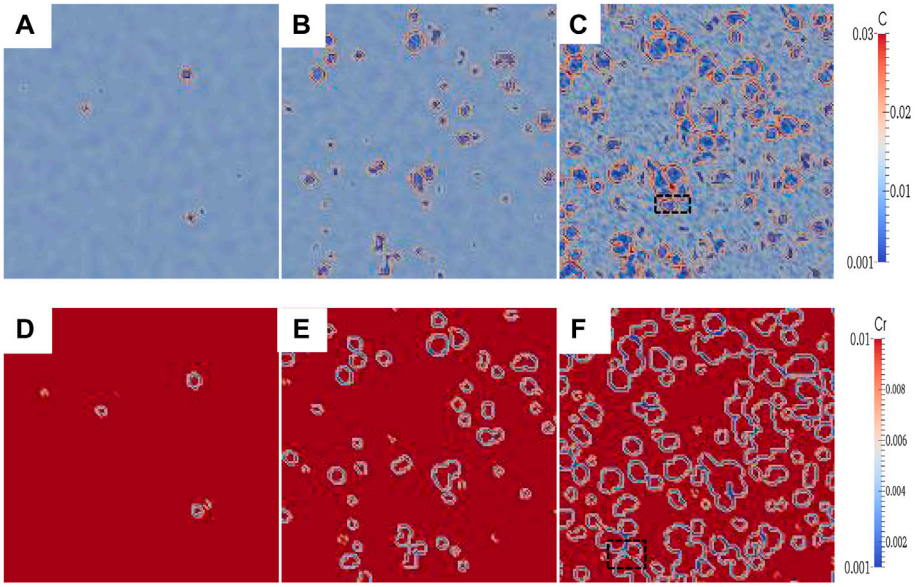

FIGURE 9
Evolution of the concentration field with time based on 1,123 K. **(A–C)** C concentration field; **(D–F)** Cr concentration field. Dimensionless time: (a, d) t* = 14; (b, e) t* = 15; (c, f) t* = 16.

$$\frac{\{c_i(r,t)\}_k^{n+1} - \{c_i(r,t)\}_k^n}{\Delta t} = -k^2 \sum_J M_{ij} \left\{ \left\{ \frac{\delta f_{local}}{\delta c_i(r,t)} \right\}_k^n + \left\{ \frac{\delta f_{el}}{\delta c_i(r,t)} \right\}_k^n + k^2 \kappa \{c_i(r,t)\}_k^{n+1} \right\} + \{\xi_{ci}(r,t)\}_k, \tag{29}$$

$$\frac{\{\phi(r,t)\}_k^{n+1} - \{\phi(r,t)\}_k^n}{\Delta t} = -k^2 \left\{ \left\{ \frac{\delta f_{local}}{\delta \phi(r,t)} \right\}_k^n \right\} - k^2 L \kappa \{\phi(r,t)\}_k^{n+1} + \left\{ \xi_\phi(r,t) \right\}_k, \tag{30}$$

where Δt represents the increment of time. In the calculation process, when the thermal fluctuations meet the Gaussian distribution, the random matrices can be randomly superimposed with the variables field, and the calculation process can be simplied. Eqs. 31, 32 have been derived. They simplify the problem of the C-H and A-C equations in the solution model to the concentration field and phase-field problems:

$$\{c_i(r,t)\}_k^{n+1} = \frac{\{c_i(r,t)\}_k^n - \Delta t k^2 \sum_j M_{ij} \left\{ \left\{ \frac{\delta f_{local}}{\delta c_i(r,t)} \right\}_k^n + \left\{ \frac{\delta f_{el}}{\delta c_i(r,t)} \right\}_k^n \right\}}{1 + \Delta t k^4 \{c_i(r,t)\}_k^{n+1}}, \tag{31}$$

$$\{\phi(r,t)\}_k^{n+1} = \frac{\{\phi(r,t)\}_k^n - \Delta t k^2 \left\{ \frac{\delta f_{local}}{\delta \phi(r,t)} \right\}_k^n}{1 + \Delta t k^2 \kappa L \{\phi(r,t)\}_k^{n+1}}. \tag{32}$$

Finally, the simulation results are saved in the VTK format, and the results are visualized to obtain the dynamic simulation of the phase transition process.

4.6 Simulation of the phase-field evolution of carbide growth

Red represents the precipitated carbide phase, and the matrix phase is represented by blue in Figure 8. Noise nucleation has been used in the simulation. When the dimensionless time equals 14, there are only a few $M_{23}C_6$ carbide cores in the *FCC* matrix, which indicates that the $M_{23}C_6$ phase begins to precipitate, and nucleation from the *FCC* phase, so the area fraction of the $M_{23}C_6$ phase is small. When the dimensionless time equals 15, the number of $M_{23}C_6$ carbide cores increases significantly and grows to form large round carbides or even two adjacent carbides, contacting to form rod carbides due to their own growth, as shown in Figure 8B. With the continuous precipitation and growth of carbides, the adjacent carbides would gradually approach until merging, and plate-like carbides and even irregular carbides would be formed, as shown in Figure 8C. It could analyze the formation mechanism of the $M_{23}C_6$ carbide from the simulation result for the mono-nuclear $M_{23}C_6$ carbide itself; carbide would grow. When two or more $M_{23}C_6$ carbide core phases contact each other, necking could occur. This argument has been verified in the following comparison with SEM images. When the two carbide phases contact each other, the total free energy of the system decreases, the contact surface

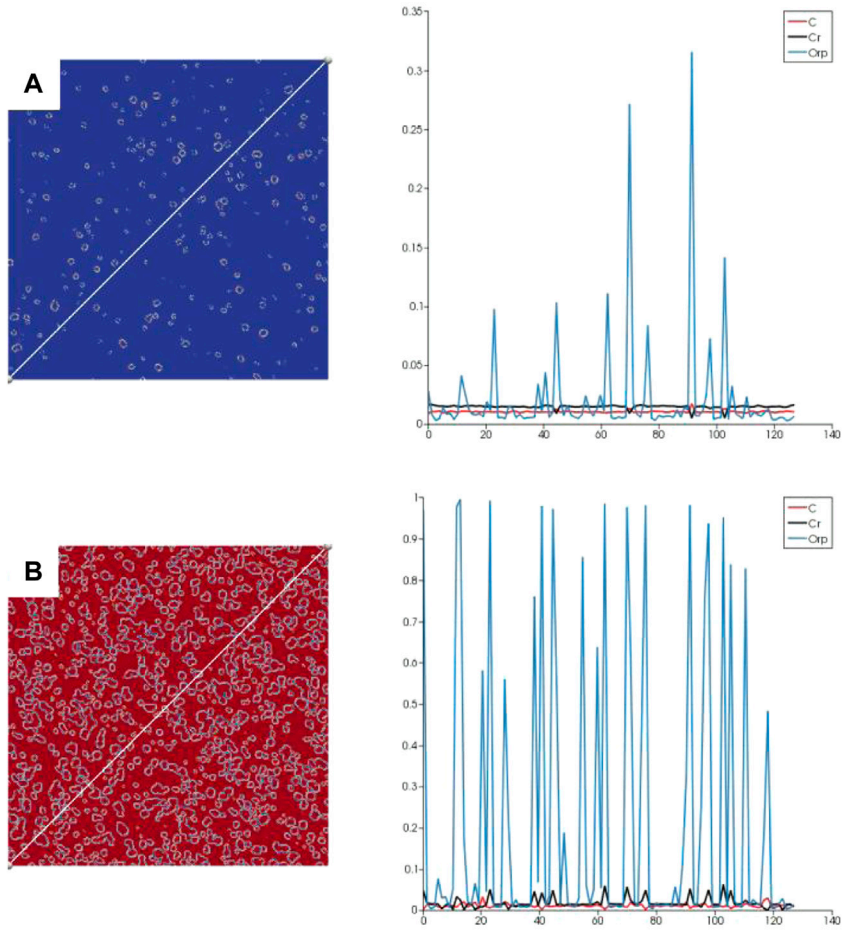

FIGURE 10
Concentration *versus* time curve along the concentration field diagonal. **(A)** Carbon concentration field. **(B)** Cr concentration field.

shrinks inward, and the specific surface area decreases, causing necking. With the continuous aging time, a series of irregular carbides could be formed.

4.7 Concentration field evolution

Figure 9 shows the change in the concentration field with time. The initial temperature equals 1,123 K, corresponding to the precipitation process of the $M_{23}C_6$ phase in Figure 8. It represents the change in the *C* concentration with time from Figures 9A–C and the change in the *Cr* concentration with time from Figures 9D–F. Dimensionless time is consistent with Figure 8. By comparing with Figure 8, it can be observed that the precipitated $M_{23}C_6$ carbides have a shell structure. Chromium is mainly concentrated in the inner layer, and the outer layer is mainly a carbon-rich area. In the process of carbide precipitation, the chemical composition in the matrix will also change accordingly. Iron, chromium, and carbon atoms could diffuse in different directions. Iron atoms could diffuse from carbide to matrix, whereas carbon and chromium atoms could diffuse from matrix to carbide (Wieczerzak et al., 2016). When multiple carbides in the matrix contact each other, there would be a carbon concentration enrichment zone and a chromium concentration depletion zone at the phase interface because carbon atoms tend to diffuse toward the interface, whereas chromium atoms diffuse in the opposite direction. Figure 10 shows the curve distribution of each phase along the diagonal of the concentration field. Orp represents M32C6 carbide phase.

5 Experimental and simulation comparison

5.1 SEM experimental study on $M_{23}C_6$ carbides

Figure 11A1 shows that many round carbides exist in the matrix for the neutral surface of the quenched part. By local amplification, it

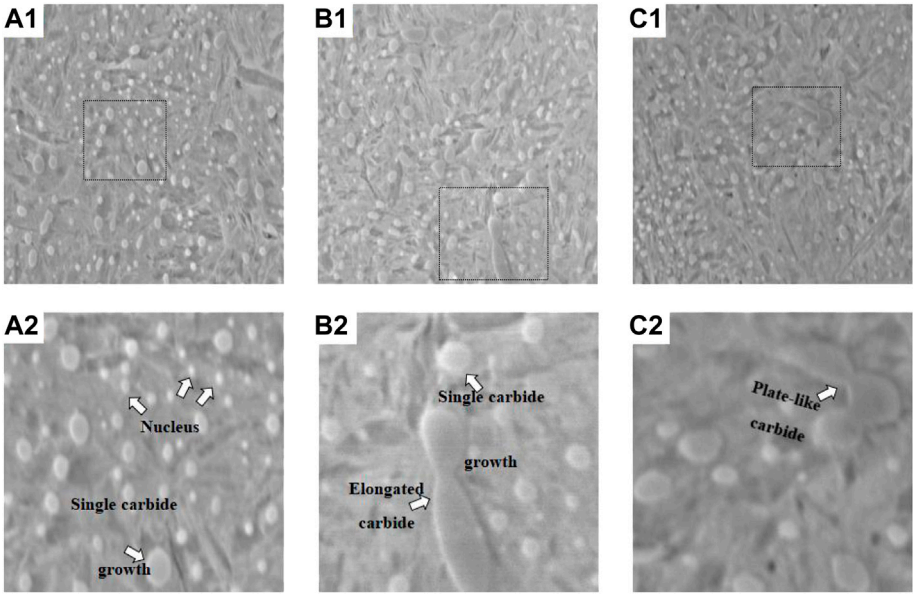

FIGURE 11
Microstructure of the GCr15 bearing outer ring quenched at different positions. **(A1)** Neutral surface of the quenched part. **(B1)** Outer surface of the quenched part. **(C1)** Inner surface of the quenched part. **(A2)** Local amplification of the neutral surface. **(B2)** Local amplification of the outer surface. **(C2)** Local amplification of the inner surface.

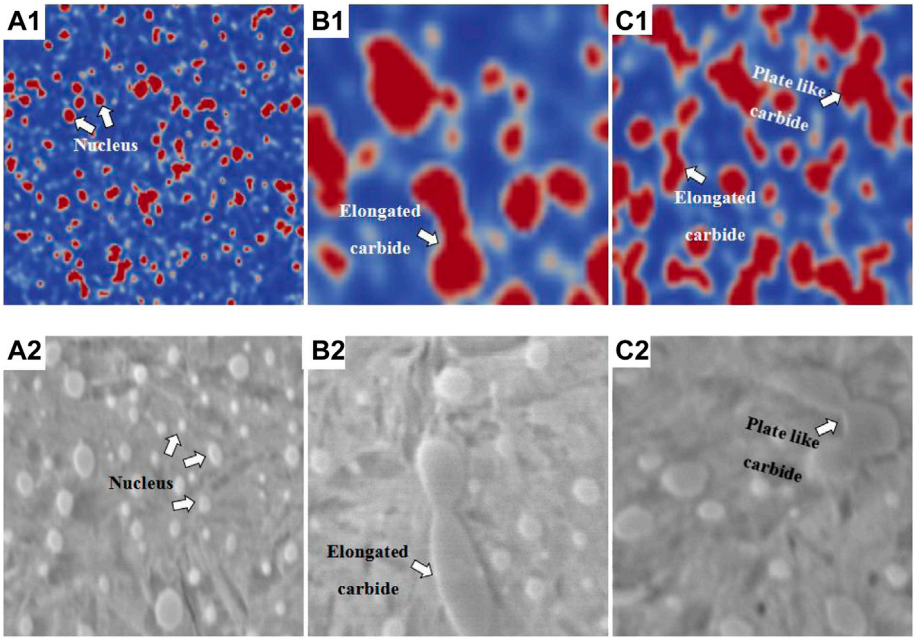

FIGURE 12
Comparison of phase-field simulation results with SEM experimental results.

could be observed that, in addition to several round carbides, there are some single coarse and short rod carbides. As a result, the $M_{23}C_6$ carbides are distributed uniformly, which is affected by the cooling rate during quenching. The heat transfer mode of the neutral surface is mainly heat conduction, without direct contact with the oil.

As shown in Figures 11B1,C1, in addition to the existence of round and short rod-like carbides, a small amount of elongated rod-like and a few irregular $M_{23}C_6$ carbides exist in the matrix for the outer and inner surfaces of the quenched part. By local amplification, it could be observed that necking occurred. The existence of a few irregular $M_{23}C_6$ carbides is due to direct contact with oil and a rapid cooling rate during quenching.

Figure 12A1 represents the phase-field simulation results of the $M_{23}C_6$ phase structure field. Figures 12B1,C1 represent the local amplification diagrams at different locations of the phase-field simulation results. The purpose is to clearly observe the $M_{23}C_6$ phases with different characteristics. Figures 12A2,B2,C2 represent the local magnification of the microstructure of the neutral, outer, and inner surfaces of the quenched part, respectively. Round, rod, plate-like, and elongated $M_{23}C_6$ carbides shown in the simulation results can be observed in the SEM results. The cooling rate could affect $M_{23}C_6$ carbide precipitation and growth, combined with experimental results. The mechanism of $M_{23}C_6$ carbide precipitation has already been verified. It indicates that the experimental results agree with the phase-field simulation results, proving the feasibility of the phase-field simulation method. Rapid cooling has accelerated the precipitation and growth of $M_{23}C_6$ carbides. The growth rate causes contact between adjacent carbides and eventually merges; rod, plate-like, elongated, and even a few nonuniform formal $M_{23}C_6$ carbides have been formed easily. Therefore, round-shaped $M_{23}C_6$ carbides have been precipitated and formed on the neutral surface of the quenched part because of the slow cooling rate, which has been caused by indirect contact with oil. However, $M_{23}C_6$ carbides show a variety of shapes in the outer and inner surfaces of the quenched part. Direct contact with oil brings more possibilities. How to control the cooling rate of quenching and contact area with oil to optimize $M_{23}C_6$ carbide precipitation and the growth state remains unexplored.

6 Conclusion

By compared the simulation results with the SEM results, we can judge the formation mechanism of carbide; for mono-nuclear carbide itself, carbide would grow. When two or more carbide core phases contact each other, necking could occur. This argument has been verified in comparison with SEM results. When the two carbide phases contact each other, the total free energy of the system decreases, the contact surface shrinks inward, and the specific surface area decreases, causing necking. With the continuous aging time, a series of irregular carbides could be formed.

The cooling rate in quenching could affect $M_{23}C_6$ carbide precipitation and growth, combined with experimental results. Rapid cooling has accelerated the precipitation and growth of $M_{23}C_6$ carbides, the growth rate causes contact between adjacent carbides, and eventually merges; rod, plate-like, elongated, and even a few nonuniform formal $M_{23}C_6$ carbides have been formed easily. How to control the cooling rate of quenching and contact area with oil to optimize $M_{23}C_6$ carbide precipitation and growth state remains unexplored.

It indicates that the experimental results agree with the phase-field simulation results, proving the feasibility of the phase-field simulation method used. Meanwhile, the difference between the parameters selected in the phase-field simulation and the true value may lead to errors in the analysis results. Further optimization of the phase-field model is the direction of future efforts.

Data availability statement

The original contributions presented in the study are included in the article/Supplementary Material; further inquiries can be directed to the corresponding author.

Author contributions

Conceptualization: MC and DJ. Methodology: QL and JJ. Software: MC and DJ. Validation: QL and JJ. Formal Analysis: JJ and QL. Experiment: QL. Investigation: MC and DJ. Resources: MC and DJ. Data curation: XD and JW. Supervision: MC and DJ. Writing—original draft preparation: JJ and QL. Writing—review and editing: QL and JJ. Project administration: DJ. All authors read and agreed to the published version of the manuscript.

Funding

This research was funded by the National Key Research and Development Project (2018YFE0207000).

Acknowledgments

The authors thank ChangZhou NRB Corporation in China and the High-Tech Research Center at the Saitama Institute of Technology in Japan for the related experiments.

Conflict of interest

The authors declare that the research was conducted in the absence of any commercial or financial relationships that could be construed as a potential conflict of interest.

Publisher's note

All claims expressed in this article are solely those of the authors and do not necessarily represent those of their affiliated organizations, or those of the publisher, the editors, and the reviewers. Any product that may be evaluated in this article, or claim that may be made by its manufacturer, is not guaranteed or endorsed by the publisher.

References

Andersson, J. O . (1988). A thermodynamic evaluation of the Fe-Cr-C system. *J.* 19 (3), 627–636. doi:10.1007/bf02649276

Andersson, J. O . (1987). Thermodynamic properties of Cr-C. *Calphad* 11, 271–276. doi:10.1016/0364-5916(87)90045-9

Cahn, J. W., and Hilliard, J. E. (1958). Free energy of a nonuniform system. I. Interfacial free energy. *J. Chem. Phys.* 28 (2), 258–267. doi:10.1063/1.1744102

Chen, L. Q., and Jie, S. (1998). Applications of semi-implicit Fourier-spectral method to phase field equations. *Comput. Phys. Commun.* 108 (2-3), 147–158. doi:10.1016/s0010-4655(97)00115-x

Ding, W (2019). *Study on the evolution of residual stress during continuous cooling and annealing process of high strength steel [D]*. China, Beijing: University of Science and Technology Beijing.

Du, G (2017). *Study on the control of carbides in bearing steel GCr15 based on electroslag remelting process [D]*. China, Beijing: University of Science and Technology Beijing.

Guo, Z (2021). *Study on precipitation mechanism of Ni—rich phase in Cu-Ni-Si-Mg alloy by phase field method [D]*. Taiyuan, China: North University of China.

Gururajan, M. P., and Abinandanan, T. A. (2007). Phase field study of precipitate rafting under a uniaxial stress. *Acta Mater.* 55 (15), 5015–5026. doi:10.1016/j.actamat.2007.05.021

Hu, S. Y., Murray, J., Weiland, H., Liu, Z., and Chen, L. (2007). Thermodynamic description and growth kinetics of stoichiometric precipitates in the phase-field approach. *Calphad* 31 (2), 303–312. doi:10.1016/j.calphad.2006.08.005

Jiang, X.-A., Zhao, Y.-H., Wen-Kui, Y., Xiao-Lin, T., and Hou, H. (2022). Mechanism of internal magnetic energy of Cu-rich phase precipitation in Fe84Cu15Mn1 alloy by phase field method [J]. *Acta Phys. Sinca* 71 (8), 080201. doi:10.7498/aps.71.20212087

Jokisaari, A. M ., and Thornton, K . (2015). General method for incorporating CALPHAD free energies of mixing into phase field models : Application to the α -zirconium/δ-hydride system. *Calphad* 51, 334–343. doi:10.1016/j.calphad.2015.10.011

Kamel, B., and Hafid, A. (2013). Elastic constants of austenitic stainless steel: Investigation by the first-principles calculations and the artificial neural network approach. *Comput. Mater. Sci.* 67 (1-2), 353–358. doi:10.1016/j.commatsci.2012.09.005

Khvan, A. V., Hallstedt, B., and Broeckmann, C. (2014). A thermodynamic evaluation of the Fe–Cr–C system. *Calphad* 46, 24–33. Pergamon Press. doi:10.1016/j.calphad.2014.01.002

Kitashima, T., Yokokawa, T., Yeh, A. C., and Harada, H. (2008). Analysis of element-content effects on equilibrium segregation at γ/γ′ interface in Ni-base superalloys using the cluster variation method. *Intermetallics* 16 (6), 779–784. doi:10.1016/j.intermet.2008.02.015

Koyama, T., Hashimoto, K., and Onodera, H. (2006). Phase-field simulation of phase transformation in Fe-Cu-Mn-Ni quaternary alloy. *Mat. Trans.* 47 (11), 2765–2772. doi:10.2320/matertrans.47.2765

Koyama, T., and Onodera, H. (2005). Computer simulation of phase decomposition in Fe–Cu–Mn–Ni quaternary alloy based on the phase-field method. *Mat. Trans.* 46 (6), 1187–1192. doi:10.2320/matertrans.46.1187

Kuang, W., Wang, H., Xin, L., Zhang, J., Zhou, Q., and Zhao, Y. (2018). Application of the thermodynamic extremal principle to diffusion-controlled phase transformations in Fe-C-X alloys: Modeling and applications. *Acta Mater.* 159, 16–30. doi:10.1016/j.actamat.2018.08.008

Kučera, J., and Stránský, K. (1982). Diffusion in iron, iron solid solutions and steels. *Mater. Sci. Eng.* 52 (1), 1–38. doi:10.1016/0025-5416(82)90067-2

Laing, P G., Ferguson, A B., Jr., and Hodge, Ph.D. E S. (1967). Tissue reaction in rabbit muscle exposed to metallic implants. *J. Biomed. Mat. Res.* 1 (1), 135–149. doi:10.1002/jbm.820010113

Lee, S. J., Matlock, D. K., and Tyne, C. J. V. (2011). An empirical model for carbon diffusion in austenite incorporating alloying element effects. *ISIJ Int.* 51 (11), 1903–1911. doi:10.2355/isijinternational.51.1903

Levchenko, E. V., Evteev, A. V., Belova, I. V., and Murch, G. (2009). Molecular dynamics simulation and theoretical analysis of carbon diffusion in cementite. *Acta Mater.* 57 (3), 846–853. doi:10.1016/j.actamat.2008.10.025

Li, F (2009). *Phase-field method research on microstructure of multicomponent alloys solidification [D]*. Lanzhou, China: Lanzhou University of Technology.

Liu, Q., Ju, D., Li, X., Ishikawa, K., Lv, R., Lian, W., et al. (2022). Verification of the non-axisymmetric deformation mechanism of bearing rings after quenched in a multi-field coupled simulation. *Coatings (Basel).* 12 (5), 676. doi:10.3390/coatings12050676

Liu, Y., Jiang, Y., Xing, J., Zhou, R., and Jing, F. (2015). Mechanical properties and electronic structures of M23C6 (M = Fe, Cr, Mn)-type multicomponent carbides. *J. Alloys Compd.* 648, 874–880. doi:10.1016/j.jallcom.2015.07.048

Loginova, I., Odqvist, J., Amberg, G., and Agren, J. (2003). The phase-field approach and solute drag modeling of the transition to massive γ → α transformation in binary Fe-C alloys. *Acta Mater.* 51 (5), 1327–1339. doi:10.1016/s1359-6454(02)00527-x

Saunders, N., and Miodownik, A. P. (1992). *Calphad (calculation of phase diagrams) A comprehensive guide[J]*. pergamon: Elsevier.

Song, W, Choi, P-P, Inden, G, Prahl, U, Raabe, D, and Bleck, W (2014). On the spheroidized carbide dissolution and elemental partitioning in high carbon bearing steel 100Cr6. *Metall. Mat. Trans. A* 45, 595–606. doi:10.1007/s11661-013-2048-5

Sun., Y. (2020). *Effects of elastic field and microelements on the precipitation of Cu-rich phase in Fe-Cu-Mn-Ni-A1 quinary alloy: A phase-field study [D]*. Taiyuan, China: North University of China.

Tian, X., Zhao, Y., Gu, T., Guo, Y., Xu, F., and Hou, H. (2022). Cooperative effect of strength and ductility processed by thermomechanical treatment for Cu–Al–Ni alloy. *Mater. Sci. Eng. A* 849, 143485. doi:10.1016/j.msea.2022.143485

Wheeler, A. A., Boettinger, W. J., and Mcfadden, G. B. (1992). Phase-field model for isothermal phase transitions in binary alloys. *Phys. Rev. A . Coll. Park.* 45 (10), 7424–7439. doi:10.1103/physreva.45.7424

Wieczerzak, K., Bala, P., Dziurka, R., Tokarski, T., Cios, G., Koziel, T., et al. (2016). The effect of temperature on the evolution of eutectic carbides and M 7 C 3 → M 23 C 6 carbides reaction in the rapidly solidified Fe-Cr-C alloy. *J. Alloys Compd.* 698, 673–684. doi:10.1016/j.jallcom.2016.12.252

Wu, M. (2021). *Hot deformation behavior, microstructure and property of super duplex stainless steel S32750 [D]*. Taiyuan, China: Taiyuan University of Technology.

Xin, T., Zhao, Y., Mahjoub, R., Jiang, J., Yadav, A., Nomoto, K., et al. (2021). Ultrahigh specific strength in a magnesium alloy strengthened by spinodal decomposition. *Sci. Adv.* 7 (23), eabf3039. doi:10.1126/sciadv.abf3039

Zhang, J. B., Wang, H. F., Kuang, W. W., Zhang, Y. H., Li, S., Zhao, Y. H., et al. (2018). Rapid solidification of non-stoichiometric intermetallic compounds: Modeling and experimental verification. *Acta Mater.* 148, 86–99. doi:10.1016/j.actamat.2018.01.040

Zhao, Y., Liu, K., Hou, H., and Chen, L-Q. (2022). Role of interfacial energy anisotropy in dendrite orientation in Al-Zn alloys: A phase field study. *Mater. Des.* 216, 110555. doi:10.1016/j.matdes.2022.110555

Zhao, Y. (2022). Stability of phase boundary between L12-Ni3Al phases: A phase field study. *Intermetallics* 144, 107528. doi:10.1016/j.intermet.2022.107528

Zhao, Y., Sun, Y., and Hou, H. (2022). Core-shell structure nanoprecipitates in Fe-xCu-3.0Mn-1.5Ni-1.5Al alloys: A phase field study. *Prog. Nat. Sci. Mater. Int.* 32 (3), 358–368. doi:10.1016/j.pnsc.2022.04.001

Zhao, Y., Zhang, B., Hou, H., Chen, W., and Wang, M. (2019). Phase-field simulation for the evolution of solid/liquid interface front in directional solidification process. *J. Mater. Sci. Technol.* 35 (6), 1044–1052. doi:10.1016/j.jmst.2018.12.009

Zhao-kun, L., Jian-zhong, L., Xu, H., Yu, F., Dong, H., and Wen-quan, C. (2016). Current status and development trend of bearing steel in China and abroad [J]. *J. Iron Steel Res.* 28 (3), 1–12. doi:10.13228/j.boyuan.issn1001-0963.20150345

Zhu, J. Z., Wang, T., Ardell, A. J., Zhou, S., Liu, Z., and Chen, L. (2004). Three-dimensional phase-field simulations of coarsening kinetics of γ′ particles in binary Ni–Al alloys. *Acta Mater.* 52 (9), 2837–2845. doi:10.1016/j.actamat.2004.02.032

Zhu, N. Q., He, Y. L., Liu, W. Q., L, L., Huang, S. G., Vleugels, J., et al. (2011). Modeling of nucleation and growth of $M_{23}C_6$ carbide in multi-component Fe-based alloy. *J. Mater. Sci. Technol.* 27 (8), 725–728. doi:10.1016/s1005-0302(11)60133-3

Zong, N., Huang, J., Liu, J., Lu, Z., and Jing, T. (2020). Present situation and prospect of Key metallurgical technologies for improving quality of bearing steel [J]. *Bearing* (12), 60–66. doi:10.19533/j.issn1000-3762.2020.12.013

Zou, W. (2021). Surface defect analysis of GCr15 bearing steel parts [J]. *Fujian Metall.* 50 (4), 37–40. doi:10.3969/j.issn.1672-7665.2021.04.010